#### **Research Article**

Wanfu Guo, Youping Yi, Jinhua Ruan, and Changming Liu\*

# Effects of cold deformation modes on microstructure uniformity and mechanical properties of large 2219 Al–Cu alloy rings

https://doi.org/10.1515/rams-2023-0124 received June 06, 2023; accepted September 18, 2023

Abstract: The mechanical properties of large 2219 Al-Cu alloy rings need to be further improved with the diameter of the launch vehicle being more than 10 m. In this study, the effects of cold rolling (CR) and cold compression on microstructure evolution and the comprehensive mechanical properties of such rings were compared. The evolution of dislocation characteristics, grain structure, second phase, and the mechanical properties of the T8-aged samples were examined. Results show that compared with CR, because of deformation characteristics, cold compression deformation induces less increase in dislocation densities; however, the increase in dislocation densities on the core was higher than at other positions, resulting in a more uniform grain structure and elongation in the axial and radial direction. The cold compression deformation contributes to the uniform dissolution of the secondary phase, resulting in denser precipitates, and thus improved strength. Brittle fractures occur in fewer CR samples because of the longer moving distance of the Al matrix. In summary, both CR and cold compression can improve the mechanical properties. However, the coldcompressed sample exhibits more uniform microstructure and higher comprehensive mechanical properties (the radial elongation increased from 7.1 to 11.2%; the in-plane

**Keywords:** cold deformation, grain structures, second phases

## 1 Introduction

With the development of space exploration, the diameter of the launch vehicle is more than 10 m, and the tank transition ring, which is the core component connecting the tank and the rocket body, has a higher mechanical property index [1]. Previous studies show that cold deformation is a highly effective method, which can be used to greatly change the microstructure of the 2219 Al–Cu alloy [2,3]. Based on the original manufacturing process, the additional cold deformation can lead to the formation of fine grains and crystalline phases, improving the comprehensive mechanical properties of rings. However, different cold deformation modes exhibit different deformation characteristics, and the microstructure evolution of cold deformation is complex and difficult to control [4,5].

The microstructure and mechanical properties of Al alloy can be fully changed by deformation via cold compression [6,7]. Lu et al. [8] performed multidirectional axial compression of a 2297 Al alloy sheet at 160°C to induce different cumulative strains. The results show that the tensile strength of the sheets increases from 267 to 480 MPa due to the higher density and smaller precipitated phase of the new dislocations. Due to the destruction of the dislocated structures by the high-strain deformation mode, a large amount of precipitated phase should be located in the original dislocation, so the size of the precipitated phase is effectively reduced. The smaller precipitated phase also attenuates the local hardening during the tensile process and also yields a higher elongation (11.2%). Dong et al. [9] studied the effects of ultra-low-temperature compression on the second-phase particles of 2219 aluminum alloy. The results show that the ultra-low-temperature compression disrupts the coarse second-phase particles significantly.

Wanfu Guo, Jinhua Ruan: Key Laboratory of Metallurgical Equipment and Control Technology, Ministry of Education, Wuhan University of Science and Technology, Wuhan 430081, China; Hubei Key Laboratory of Mechanical Transmission and Manufacturing Engineering, Wuhan University of Science and Technology, Wuhan 430081, China Youping Yi: State Key Laboratory of High Performance Complex Manufacturing, Central South University, Changsha 410083, China

anisotropy decreased from 36.6 to 8.9%), without any brittle fractures, because of more uniform metal flow.

<sup>\*</sup> Corresponding author: Changming Liu, Key Laboratory of Metallurgical Equipment and Control Technology, Ministry of Education, Wuhan University of Science and Technology, Wuhan 430081, China; Hubei Key Laboratory of Mechanical Transmission and Manufacturing Engineering, Wuhan University of Science and Technology, Wuhan 430081, China, e-mail: liuchangming@wust.edu.cn

2 — Wanfu Guo et al. DE GRUYTER

The crystalline phase is more soluble in the matrix, which enhances precipitation and reduces the stress concentration in the matrix, resulting in a significant improvement in the mechanical properties of the alloy.

Cold rolling (CR) is another conventional cold deformation mode [10,11]. Changela *et al.* [12] reported that constrained groove pressing, followed by CR, is an effective alternate route to produce Al alloy sheets with ultra-fine microstructure. The 4.7  $\mu$ m fine crystal Al-6.5 Mg alloy was prepared by high strain rate hot rolling at 400°C, resulting in a combination of low ultimate strength (354 ± 1 MPa) and high elongation (34 ± 0.9%). After subsequent CR treatment, the ultimate strength was further increased to 454 ± 2 MPa, and the ductility was 9.2 ± 1.1%. The strength improvement was mainly due to the combination of strain hardening, grain refinement, and high Mg content because of additional solute during CR.

Some studies were about the comparison of deformation behaviors of cold compression and CR [13]. First, the deformation mechanisms were studied. By comparing the deformation process and crystal orientation characteristics of rolling and compression deformation, Fujita et al. [14,15] found that the metal flow for the two deformation modes was very different. Rolling was the surface material extending around unevenly, and compression was the intermediate material extending outwards. In addition, the textures formed in the uniaxially compressed rod and rolled sheet are not similar. On the other hand, the focus was on the differences in microstructures and mechanical properties caused by two such modes of deformation. The effects of cold stretching and cold compression on the microstructure evolution and strong plasticity of Al-Cu-Mg-Si alloy were compared [16]. Compared with no deformation, the sample with 4% cold compression had a finer  $\theta'$  phase, higher dislocation density, and larger contact angle of Al<sub>2</sub>Cu phases, resulting in higher strength and lower plasticity. Compared with 4% cold compression, the proportion of the  $\theta'$  phase of the cold stretching sample was higher and the contact angle of the Al<sub>2</sub>Cu phase was smaller. Therefore, the cold stretching sample of Al-Cu-Mg-Si alloy exhibits higher strength and plasticity.

Guo et al. [17,18] adopted cold compression and CR to induce the deformation of large 2219 Al–Cu alloy rings. Both cold deformation modes cause large accumulation of dislocations, contributing to grain refinement and dissolution of the Al<sub>2</sub>Cu phase, and improved strength and plasticity of the ring. However, the two deformation modes had different effects on the ring microstructure and mechanical properties. In order to further accurately control the microstructure and mechanical properties of the ring, this study compared the effects of two cold deformation modes

on the microstructure evolution and comprehensive mechanical properties of the large ring, and the effects of different cold deformations on the microstructure and properties of the ring were fully explored. This study focused on the variation in dislocation density under cold deformation, the grain structure of different parts, the dissolution behavior of the second phase in the solution after cold deformation, and the subsequent aging precipitation to further analyze the mechanical behavior.

## 2 Experimental procedure

The elemental composition of the 2219 Al–Cu alloy is shown in Table 1. Figure 1 shows the process of cold deformation comparison of the 2219 Al–Cu alloy. The test method is shown in Figure 2, and the process parameters are presented in Table 2. A sample with dimensions of 135 (circumferential direction)  $\times$  220 (radial direction)  $\times$  135 (axial direction) mm was cut from the  $\Phi$ 1,200 mm 2219 Al alloy ingots. The samples were billeted by multi-direction forging first, followed by warm rolling at 240°C/25%. The single rolling pressure was 4.0 mm, which simulated the

**Table 1:** The chemical composition of the 2219 Al alloy used in this test (wt%)

Si	Fe	Cu	Mn	Mg	Zn	٧	Ti	Zr	Al
0.2	0.3	6.02	0.40	0.02	0.1	0.08	0.08	0.12	Bal

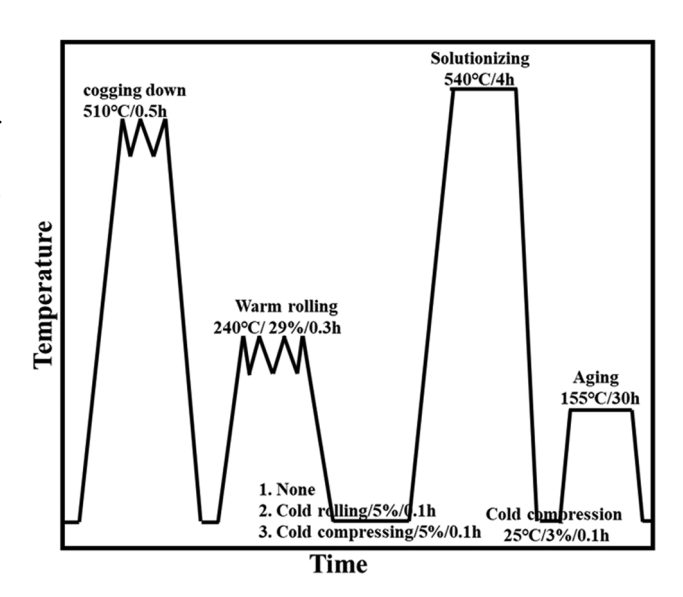


**Figure 1:** Experimental process of the cold deformation comparison.

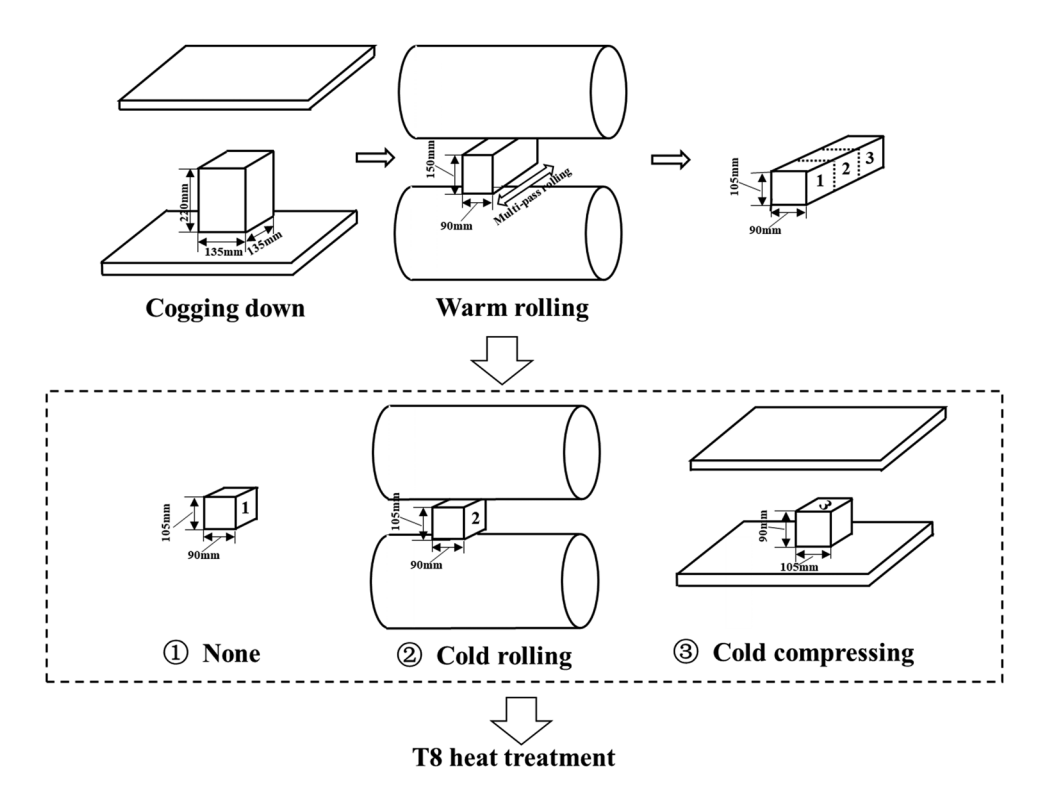


Figure 2: Experimental method of the cold deformation comparison.

real ring rolling process, followed by cold deformation. According to the shape characteristics of the application object, a large ring, the selected cold deformation mode involved radial CR and axial cold compression. The three specific terms of comparison include no cold deformation, CR deformation, and cold compression deformation, with an overall deformation of 5%. The subsequent heat treatment (T8) entailed solution treatment for 4 h at 540°C, followed by water quenching and deformation *via* cold compression (3%). After cold deformation, they were directly transferred to the aging furnace for 30 h at 155°C.

The corresponding directions and positions of each sample are shown in Figure 3. The tensile tests were conducted on the WDW-100A universal testing machine with a tensile speed of 2.0 mm·min<sup>-1</sup>. The shape of the mechanic's performance testing sample is shown in Figure 4. Tensile tests based on the GB-T228-2002 standard were performed in the axial, radial, and circumferential directions (AD, RD,

and CD), the tensile tests were conducted thrice in each direction, and the measured values were averaged. The grain structure of the 2219 Al–Cu alloy was analyzed with an OLYMPUS DSX500 metallographic microscope. The sample was polished using the Keller reagent (HF/HCl/HNO $_3$ /H $_2$ O = 2:3:5:190). The coarse second phase particles and fracture

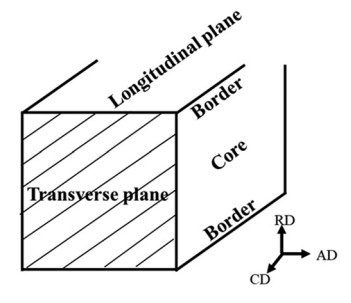


Figure 3: Positions and directions of samples.

Table 2: Parameters of cold deformation comparison

	Rolling temperature (°C)	Rolling deformation	Single rolling reduction (mm)	Cold deformation parameters	Heat treatment
1	240	25%	4.0	None	540°C*4 h solution
2				5% CR	+3% compression
3				5% CP	+155°C*30 h aging

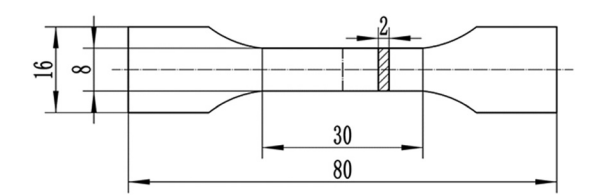


Figure 4: The shape of the mechanical property testing sample.

structure were observed and analyzed by scanning electron microscopy (SEM)(model: Phenom ProX desktop SEM); element composition of phases in the Al matrix or fracture surface and Cu content in the matrix were measured by SEM-energy dispersive spectrometer (EDS) analysis. In this experiment, dislocations and precipitation were observed and analyzed *via* Tecnai G2 F20 emission transmission electron microscopy (TEM).

## 3 Results

## 3.1 Dislocation characteristics after cold deformation

Figure 5 shows the dislocation characteristics of the Al matrix after cold deformation at the core sampling location. By scanning transmission electron microscopy-EDS analysis, the variety of secondary phases to each sample was all  $Al_2Cu$ . As shown in Figure 5(a), warm rolling induced obvious dislocations in the matrix, and intertwined dislocation lines. The secondary phase was relatively dispersed without an obvious relationship with dislocation structures.

As shown in Figure 5(b), after radial CR, a large number of dislocations accumulated locally in the Al matrix and spread across multiple regions through the dislocation wall. The sub-crystalline structures formed initially. Concurrently, many areas with lower dislocation densities were observed. No obvious interactions between the secondary phase and dislocation structures were found. As shown in Figure 5(c), after axial cold compression, obvious dislocation entanglements in most areas of the Al matrix indicated the flow of metal flows more evenly during cold compression than in CR, and a more uniform dispersion and accumulation of dislocations. The dislocation-free area around the secondary phase, namely the dislocation cell structure, indicates that the secondary phase, as a stress concentration location, can lead to the accumulation of a large number of dislocations during cold compression.

With the change in the dislocation structure, the dislocation densities also change. Table 3 shows the dislocation density (obtained by XRD analysis) of samples with different cold deformations at the core in the longitudinal section. The relationship between the relevant data obtained by XRD and the dislocation densities in the sample is represented by the following equations:

Table 3: Dislocation densities at each position

	Core (×1,014 m <sup>-2</sup> )	Quarter (×1,014 m <sup>-2</sup> )	Border (×1,014 m <sup>-2</sup> )
None	0.26 ± 0.03	0.30 ± 0.02	0.37 ± 0.02
5% CR	$0.79 \pm 0.05$	$0.86 \pm 0.09$	0.93 ± 0.10
5% CP	$0.58 \pm 0.05$	$0.52 \pm 0.07$	$0.46 \pm 0.07$

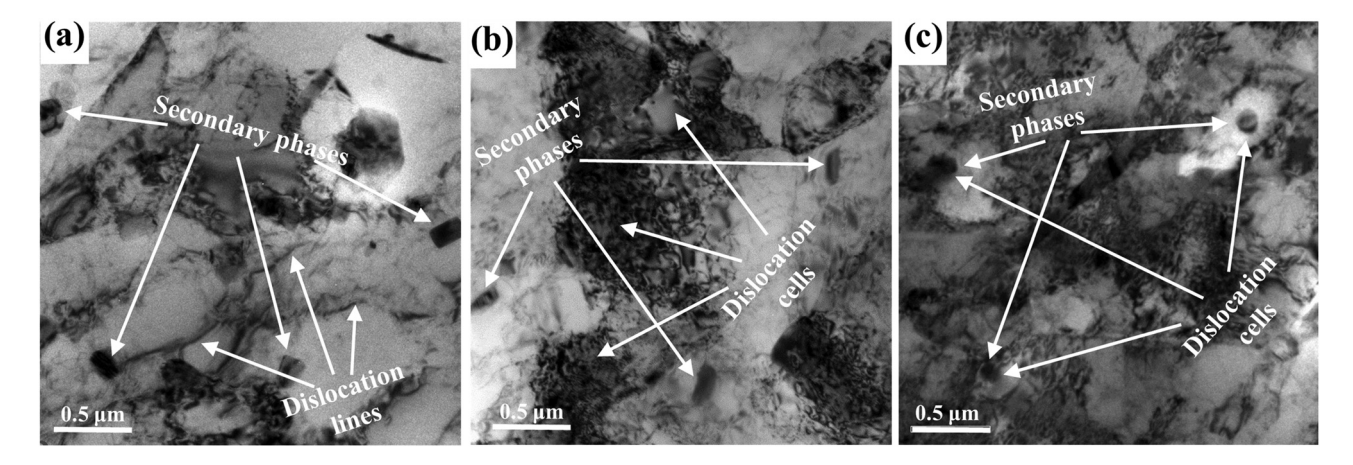


Figure 5: Dislocation structures after cold deformation. (a), (b) and (c) Cold deformation mode without deformation, 5% CR, and 5% cold compression, respectively.

$$\frac{(\delta 2\theta)^2}{\tan^2 \theta_0} = 25\langle e^2 \rangle + \frac{\lambda}{d} \left( \frac{\delta 2\theta}{\tan \theta_0 \sin \theta_0} \right), \tag{1}$$

$$\rho = \frac{2\sqrt{3} \langle e^2 \rangle^{\frac{1}{2}}}{(db)},\tag{2}$$

Here,  $\delta 2\theta$  is the half peak-width;  $\theta_0$  is the maximum position of each diffraction peak;  $e^2$  is the lattice strain; d is the size of the XRD coherent diffraction zone;  $\lambda$  (= 0.15418 nm) is the wavelength of the X-ray; b (= 0.286 nm) is the Burr vector; and  $\rho$  is the dislocation density in m<sup>-2</sup>. In  $\frac{(\delta 2\theta)^2}{\tan^2\theta_0}$  and  $\frac{\delta 2\theta}{\tan\theta_0\sin\theta_0}$ , the corresponding  $\delta 2\theta$  and  $\theta_0$  can be calculated

from the XRD data. The  $\frac{\lambda}{d}$  and  $e^2$  values are obtained by

numerical fitting, and the final  $\rho$  value can be obtained by direct substitution [19,20].

The dislocation density of the sample undergoing only warm rolling was  $0.26 \times 10^{14}$  m<sup>-2</sup>. After 5% CR deformation. the dislocation density of the sample increased greatly, reaching  $0.79 \times 10^{14} \,\mathrm{m}^{-2}$ . In comparison, the dislocation density increase by cold compression was less than that of CR, which was  $0.58 \times 10^{14}$  m<sup>-2</sup>. The results show that the dislocation density of the 2219 aluminum alloy can be significantly increased by cold deformation. The increase of CR deformation was stronger than that of cold compression. The change in the dislocation density corresponds to the change in the dislocation structure. The dislocation distribution in the matrix of the CR sample was more concentrated, and the regions of high dislocation density and free region were separated from each other. However, the dislocation distribution in the cold-compressed sample was more dispersed, and dislocations accumulated in the dispersed secondary phase. These factors contribute to the differential increase in the amplitude of dislocation densities for each sample subjected to cold deformation. In addition, the standard deviation of the dislocation density of each sample with different cold deformation modes indicate the local dislocation density uniformity of alloy after CR is lower than that of cold compression. This is related to the deformation characteristics of CR.

After radial CR and axial cold compression, the dislocation densities of the 2219 Al–Cu alloy changed significantly peripherally, and at quarter and core positions. Table 3 shows dislocation density values. In the case of the undeformed sample, the dislocation densities of the core, quarter, and edge increased successively, and the increment from the periphery to the quarter position was large, which is consistent with the distribution of flow stress during warm rolling, indicating the minor change in the deformation from the core to the quarter, and the large change from the quarter to the periphery

during warm rolling. Exposure to 5% radial CR substantially increased the dislocation densities of different components, and the increase in amplitude was relatively similar, indicating uniformity of CR deformation, and the uniform increase in the dislocation density of different sample components. Exposure to 5% axial cold compression increased the dislocation densities of different parts, with a maximum increase in the core, followed by the quarter, and the periphery, indicating that the cold compression contributed to the increased core deformation. Compared with CR deformation, the deformation induced by cold compression effectively improved the dislocation densities of the core. However, the core dislocation densities were lower in the absence of cold deformation, which led to uniform dislocation densities of the cold-compressed sample.

## 3.2 Grain structure characteristics after heat treatment

After heat treatment, each sample recrystallized completely. Figure 6 shows the grain structures of the sample periphery and core under different cold deformation modes. Table 4 presents the statistical results of the grain size. The average grain size of the sample without cold deformation was coarse (>162.0 µm). The grain size at the periphery was obviously finer than at the core, with a difference of 36.0 µm. Under 5% radial CR deformation, the average diameter of the grain at the periphery and core decreased by more than 50.0 µm. The difference in size between the periphery and the core decreased to 24.0 µm. Under 5% axial cold compression, the grain diameters at both the periphery and the core also decreased. The grain diameters of the core decreased greatly, while the grain diameters at the periphery decreased slightly. The difference in grain diameter between the border and the core was only 8.0 µm, and the grain structure uniformity greatly improved. In addition, comparing the aspect ratio of the three samples, it can be seen that after cold deformation, the equiaxial degree of grains at each position showed little change.

The statistical results of the grain size are basically consistent with the dislocation densities of each position, indicating the effectiveness of the method for refining grain structure of the 2219 Al–Cu alloy *via* cold deformation and additional dislocation. Cold compression is preferential because of the larger increase in the degree of deformation at the core, which is contrary to the effects of warm rolling. Thus, it improved the uniformity of the grain structure.

6 — Wanfu Guo et al. DE GRUYTER

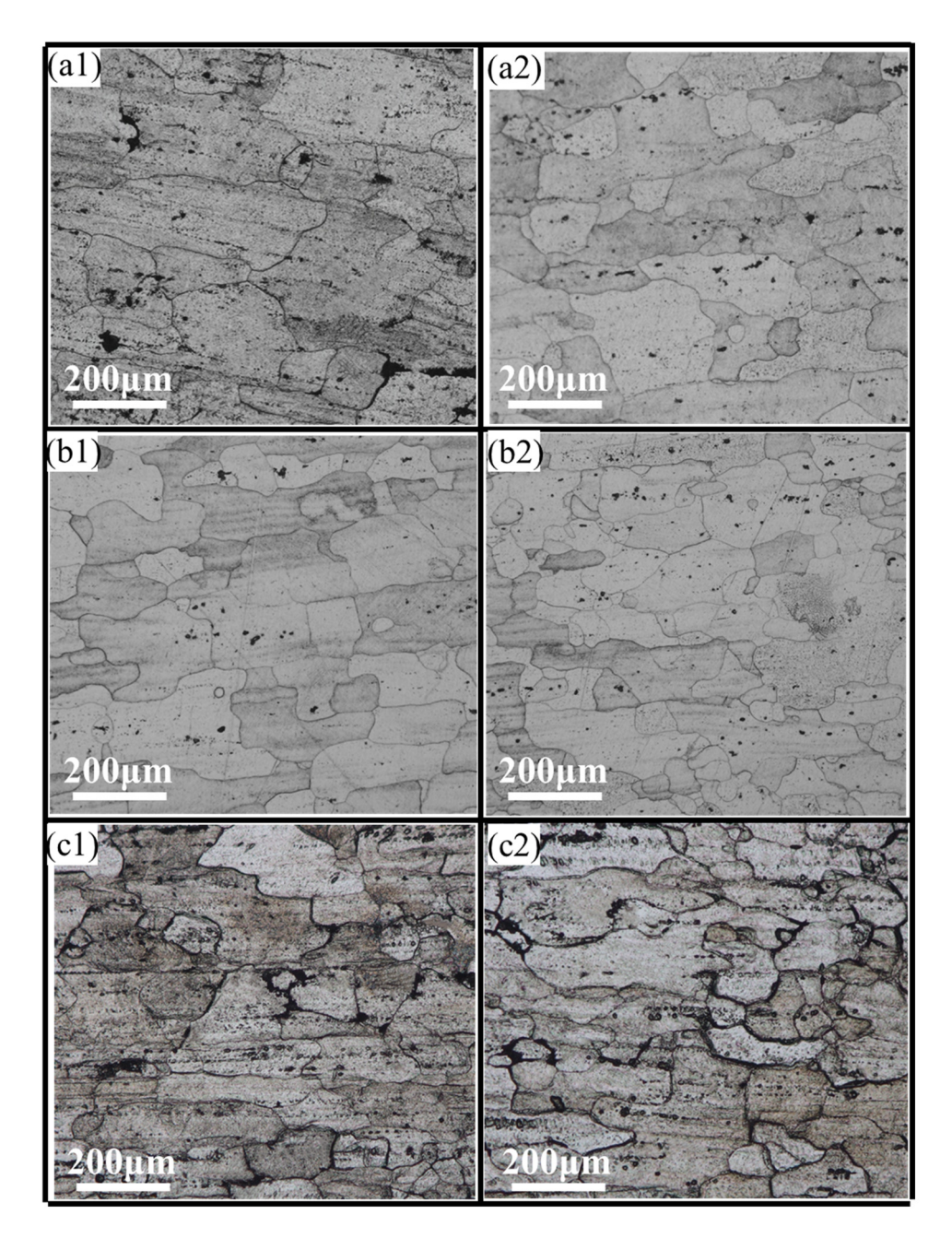


**Figure 6:** Grain structures of the sample under different cold deformations. (a1), (b1), and (c1) Longitudinal (core) grain structures in the absence of deformation, in the presence of CR, and cold compression, respectively. (a2), (b2), and (c2) Longitudinal (peripherally) grain structures in the absence of deformation, in the presence of CR, and cold compression, respectively.

 Table 4: Statistical results of the grain size

		Grain size		Aspect ratio of grains			
	Core (µm)	Border (µm)	Difference (µm)	Core (µm)	Border (µm)	Difference (µm)	
None	198.0 ± 25.0	162.0 ± 22.0	36.0	1.5	1.4	0.1	
5% CR	137.0 ± 14.0	113.0 ± 13.0	24.0	1.5	1.5	0	
5% CP	146.0 ± 20.0	138.0 ± 18.0	8.0	1.5	1.4	0.1	

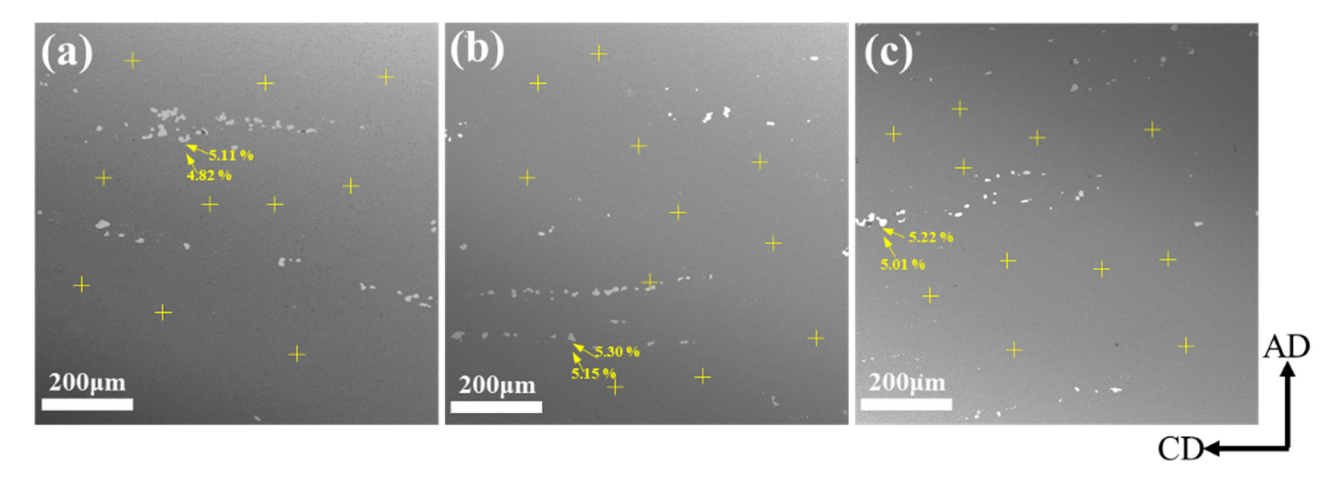


Figure 7: Al<sub>2</sub>Cu phases of the sample under different cold deformations. (a), (b) and (c) Sample with no cold deformation, 5% CR, and 5% cold compression deformation, respectively.

## 3.3 Second-phase dissolution and precipitation behavior during heat treatment

After heat treatment, the second phases of different samples undergoing cold deformation were dissolved to various degrees. Figure 7 shows the corresponding characteristics of Al<sub>2</sub>Cu phases on the core of the longitudinal section. Table 5 presents the statistical results of Cu content (SEM-EDS was used for elemental analysis); although the accuracy of this test method is not the highest, it is enough to form regular findings through obtained data from this test). In Figure 7, the Cu content in the Al matrix near the Al<sub>2</sub>Cu phase is compared. The yellow arrow points to the selected measurement point, and the two measurement points deviate from 15 µm. The Cu content in the sample matrix with 0% deformation, 5% CR, and 5% cold compression was reduced by 0.29, 0.1 and 0.21%, respectively, while the corresponding average Cu content in the matrix was 4.77, 5.03 and 4.96%, respectively. The diffusion range of Cu atoms during the dissolution was extended under cold deformation. The dissolution of the Al<sub>2</sub>Cu phase was adequate, and the Cu content in the Al matrix was increased by cold deformation. In addition, compared with cold compression, CR facilitated the increased diffusion efficiency

of Cu atoms close to coarse Al<sub>2</sub>Cu phases during the dissolution process.

As shown in Table 5, the  $Al_2Cu$  phase diameter and area fraction of  $Al_2Cu$  phases in the matrix with 0% deformation, 5% CR, and 5% cold compression were in descending order. The diffusion behavior of Cu atoms indicates that the cold compression was more favorable to the fragmentation of  $Al_2Cu$  particles, increasing the diffusion range of Cu atoms. By cold compression process, there are more dislocations accumulation on the coarse  $Al_2Cu$  phases, and such dislocation accumulation process can make more  $Al_2Cu$  phase exceed the critical load required for fragmentation, achieve more frequent fragmentation, and lower the mean diameter.

In addition, by comparing the standard deviation of the Cu content in the Al matrix of samples under different cold deformations, it can be seen that the Cu content of the Al matrix in the 5% cold-compressed sample was the most uniform. The minimal standard deviation indicates that the cold compression contributed to the uniformity of the Cu atom diffusion during the solution treatment. The cold compression increased the number of dislocation channels enormously around the secondary phase to promote atomic diffusion, while the secondary phase distribution was relatively dense.

Table 5: Cu content in the Al matrix (%), Al<sub>2</sub>Cu phase diameter (µm) and area fraction (%)

	1	2	3	4	5	6	7	8	9	10	Mean value	Standard deviation	Al <sub>2</sub> Cu phase diameter	Area fraction of Al <sub>2</sub> Cu phases
None	5.15	4.57	4.6	5.12	5.01	5.15	4.39	4.41	4.48	4.82	4.77	±0.32	15.6	0.74
5% CR	5.27	5.07	4.75	5.19	4.83	4.63	5.24	5.33	5.21	4.82	5.03	±0.25	13.6	0.62
5% CP	4.78	4.82	4.82	5.12	5.24	5.07	4.92	4.79	4.85	5.16	4.96	±0.17	12.5	0.53

8 — Wanfu Guo et al. DE GRUYTER

Figure 8 shows the TEM images of the sample under different cold deformations after aging. Table 6 presents the statistical results of the precipitated phase sizes. The sampling location is the core. As shown in Figure 7(a2), (b2) and (c2), the selected diffraction spots were analyzed (white arrows in SAED indicate {110} and {020} directions).

Diffraction spots of  $\theta'$  and  $\theta''$  phases are observed in the selected diffraction spots of each sample. In TEM images, the coarse needle-like phase is the  $\theta'$  phase. which is also the main strengthening phase of 2219 Al–Cu alloy. (In the three-dimensional space, the  $\theta'$  phase appears as a disk shape. TEM images of only the cross section. The length of

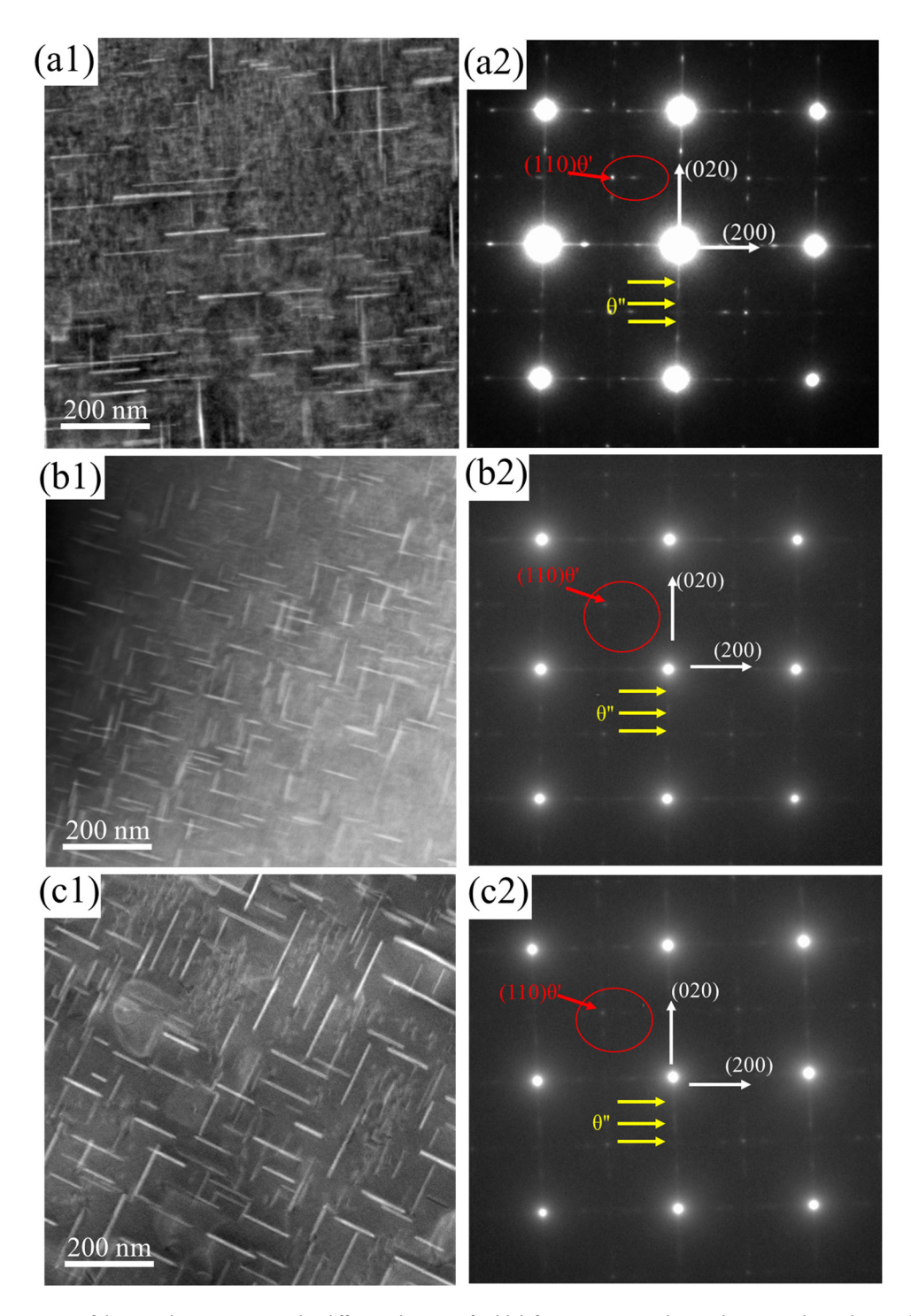


**Figure 8:** Characteristics of the sample precipitate under different degrees of cold deformations. (a1), (b1), and (c1) Samples with 0% cold deformation, 5% CR, and 5% cold compression. (a2), (b2), and (c2) Corresponding diffraction spots.

**Table 6:**  $\theta'$  phase results after T8 heat treatment

	Average volume fraction of the $ heta'$ phase (%)	Average diameter of the $\theta'$ phase (nm)	Average thickness of the $\theta'$ phase (nm)
None	8.4	147.0	6.22
5% CR	9.3	111.0	5.42
5% CP	10.8	118.0	6.20

the "needle" is the diameter of the "disk," and the width of the "needle" is the thickness of the "disk" [21,22].) When the  $\theta$  phase is dense and uniform, the yield strength of the 2219 aluminum alloy is high. The slight, dense, and needle-like phases are represented by  $\theta$ ".

Figure 8(a1) shows TEM images of samples without cold deformation, the non-uniform distribution of the  $\theta'$ phase, and an obvious precipitation-free area. The diameter is 147.0 nm, the thickness is 6.22 nm and the volume fraction is 8.4%. (The volume fraction can be obtained by multiplying the average volume by the amount of the diskshaped precipitates on the measured area, divided by the product of the area and the thickness of the measured area.) As shown in Figure 8(b1), the  $\theta'$  phase diameter of the 5% cold-rolled sample decreased to 111.0 nm and the thickness decreased to 5.42 nm. However, the  $\theta'$  phase distribution is denser and more uniform, without obvious precipitation-free region, and the volume fraction increased to 9.3%. As shown in Figure 8(c1), the  $\theta'$  phase diameter of the 5% cold-compressed sample increased to 118.0 nm, the thickness increased to 6.20 nm, and the distribution is distribution is denser and more uniform, with a volume fraction of 10.8%. The cold-compressed sample showed a greater increase in the size and a more uniform distribution of  $\theta'$  phase after heat treatment, compared to the cold-rolled sample.

Cold deformation can induce a large number of entangled dislocations around the Al<sub>2</sub>Cu phase, the dislocations act as atomic diffusion channels, can improve the dissolution of the phases, and enhance the Cu content in the Al matrix, increasing the density of the precipitated phases. Compared with CR, the dislocation structures are more inclined to wind around the secondary phases after cold compression. Because of a denser distribution of the secondary phase, and a large number of dislocations around the phases, the diffusion and range of Cu atoms in solution treatment improved greatly, enhancing Cu supersaturation in the Al matrix, and the uniform dispersion of Cu in the matrix, resulting in denser and more uniform distribution of the  $\theta'$  phase. In addition, the size of the  $\theta'$  phase also increased because of such Cu supersaturation in the Al matrix.

## 3.4 Mechanical properties and fracture behaviors

Figure 9 shows the effects of different cold deformation modes on the overall mechanical properties of large 2219 Al-Cu alloy rings. This content only reflects the axial and radial directions (with excellent circumferential performance). As shown in Figure 9(a), compared with 0% cold deformation sample, the mechanical properties were effectively improved by adding 5% cold-rolled samples. The radial yield strength increased from 310 to 368 MPa and the elongation increased from 7.1 to 8.1%. However, the tensile strength decreased significantly from 440 to 414 MPa. The axial tensile strength increased from 421 to 453 MPa; the yield strength increased from 323 to 334 MPa, while the elongation increased from 6.8 to 7.6%. Under 5% cold compression, the mechanical properties of the sample also improved significantly, with the largest increase in the yield strength and elongation of the ring. The radial yield strength increased from 310 to 358 MPa, and the elongation increased from 7.1 to 11.2%. The axial yield strength increased from 335 to 361 MPa, and the elongation increased from 11.2 to 12.3%. Both axial and radial tensile strengths improved slightly.

The mechanical properties of the samples in the current study were compared with the previous studies. Compared with the sample whose warm rolling deformation reaches 40%, the axial elongation is similar, and other mechanical property indexes have no certain advantages, indicating that the mechanical properties cannot be linearly increased by increasing the deformation amount of warm rolling [23]. Before rolling, by changing the hot forging to warm forging, severe plastic deformation is achieved; the tensile strength, yield strength, and elongation of the sample are higher than those of the current studies, especially the tensile strength and yield strength. However, due to the severe metal flow during the warm forging process, instability and cracking are likely to occur, and the warm forging needs further exploration in industry [2]. Adopting cryogenic technology to study the deformation limit and mechanical properties of the 2219 Al-Cu alloy is another exploration direction [24]. After cryogenic deformation treatment (-190°C/20%), the mechanical properties have been greatly improved compared with the normal temperature deformation, especially the tensile strength and yield strength. However, with cryogenic technology, it is difficult to realize industrial manufacturing for large components. On the contrary, the cold deformation with a small deformation amount adopted in this study is easier to realize in industrial manufacturing, having industrial application prospects. Moreover, many experiments have been carried out, including complete

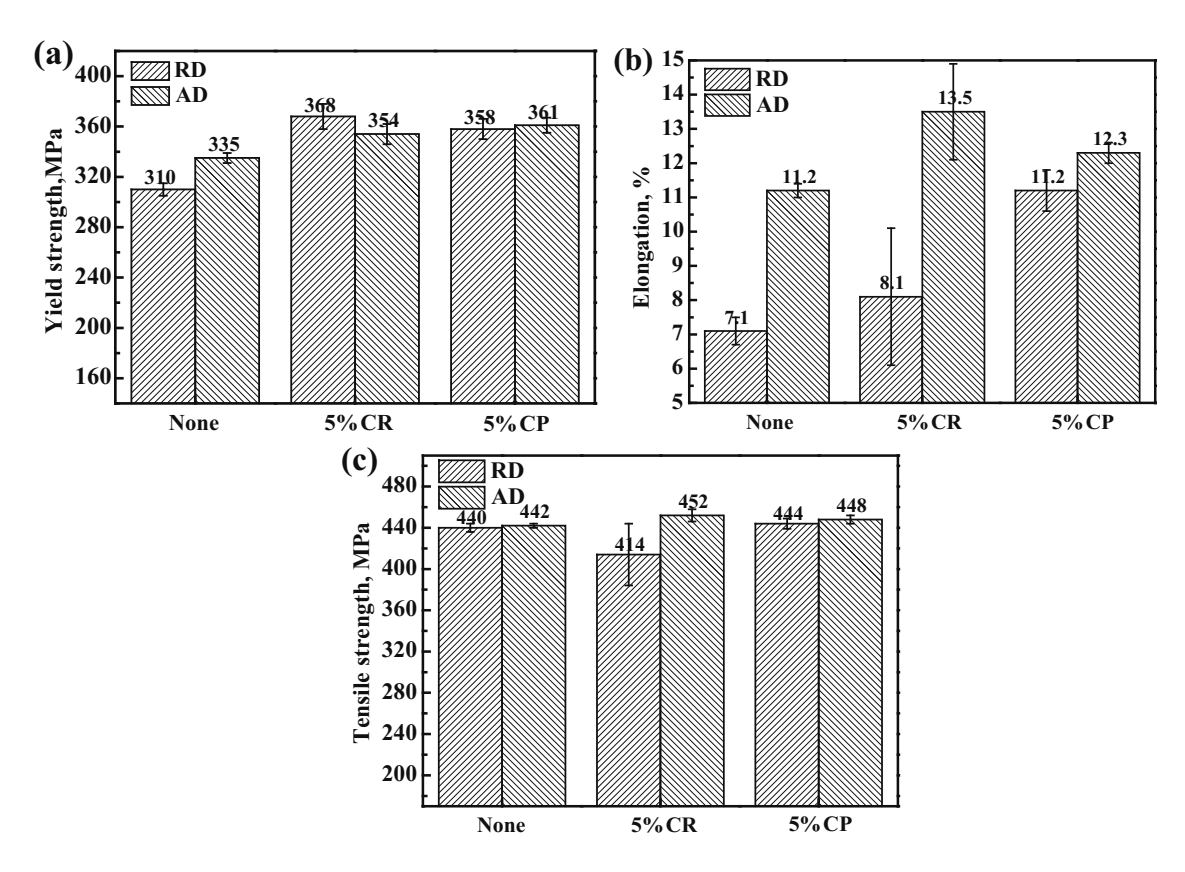


Figure 9: Mechanical properties after heat treatment: (a) yield strength, (b) elongation, and (c) tensile strength.

laboratory simulation, and selecting the samples after industrial rolling for cold deformation experiments; the evolution laws of microstructures and mechanical properties are stable [17,18].

In addition, the elongation and tensile strength of the CR samples showed large amplitude. A few positions with decreased mechanical properties appeared in the CR sample, indicating that the CR process may induce material damage within a certain range of deformation [25]. As shown in

Figure 10(a), the fracture surface included transcrystalline fracture (a large number of deep dimples and coarse  $Al_2Cu$  phases were on the bottom of the dimple) and intergranular fracture (rough grain boundary surface) characteristics, indicating conventional ductile fracture. The transcrystalline or intergranular fracture depends on whether in this area coarse phases exist. However, unexpected brittle fractures occurred, as shown in Figure 10(b), and a large number of

**DE GRUYTER** 

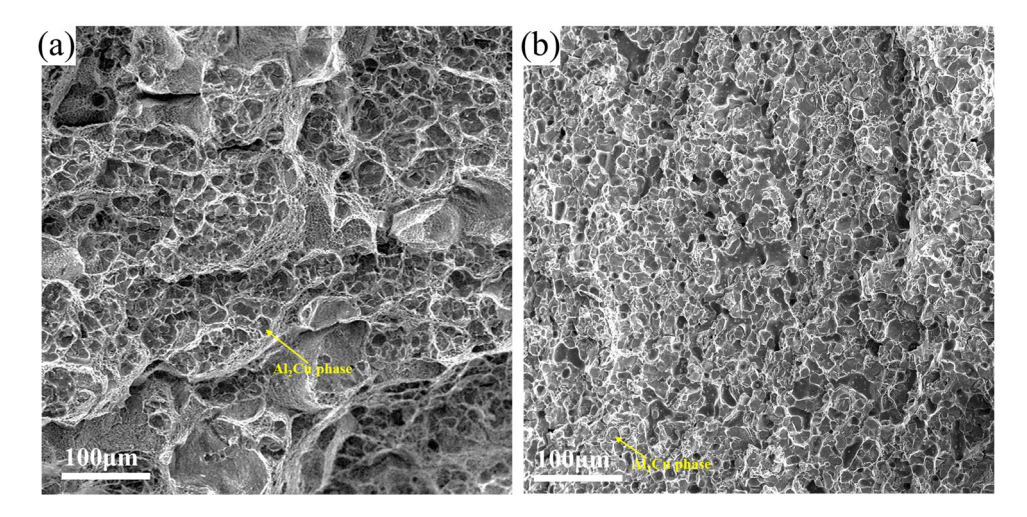


Figure 10: Fracture morphologies of the tensile samples: (a) conventional ductile fracture and (b) brittle fracture.

shallow dimples (Al<sub>2</sub>Cu phases were surrounded by shallow dimples) appeared on the fracture of a cold-rolled sample, proving the occurrence of a sort of damage [26,27].

As shown in Table 7, by comparing the in-plane anisotropy (IPA) of the samples obtained by CR and cold compression, the effect of the improved process on the ring anisotropy was determined. The IPA can be calculated as follows [28]:

IPA = 
$$\frac{2X_{\text{max}} - X_{\text{mid}}X_{\text{min}}}{2X_{\text{max}}} \times 100\%$$
. (3)

Compared with the CR sample, the IPA based on the tensile strength, yield strength, and elongation of the cold-compressed sample showed a downward trend. The IPA of the original elongation was the worst. Following process improvement *via* cold compression, the IPA significantly decreased from 36.6 to 8.9%. The results showed that the anisotropy of the cold-compressed sample was obviously weakened.

### 4 Discussion

#### 4.1 Deformation characteristics

The metal flow shows a large difference in deformation between CR and cold compression. As shown in Figure 11(a) and (b),

Table 7: Statistical results of IPA

	Yield strength (%)	Tensile strength (%)	Elongation (%)
None	7.5	0.5	36.6
5% CR	3.8	8.4	40.0
5% CP	0.8	0.9	8.9

during the rolling process, the internal particle is mainly subjected to tensile stress along the rolling direction (circumferential). However, during compression, the internal particle is subjected to both axial compression stress and tensile stress along the section perpendicular to the axial direction [13,29]. Therefore, the metal flow in CR deformation is more concentrated, while the metal flow in compression deformation is more dispersed.

In addition, because the direction of the compression deformation force is perpendicular to the direction of metal flow, the direction of the rolling deformation force is parallel to the direction of metal flow. It is difficult to transfer the force to the core. Therefore, during the rolling process, the strain at the periphery is larger than at the core. The core strain is larger than at the periphery during compression deformation. Therefore, the changes in the grain size of different components under the two deformation modes differ [30,31]. The grain structure of the sample after CR deformation is still in the state of "thin border and coarse core" after heat treatment, which is consistent with the sample undergoing zero cold deformation. Under cold compression, the grain at the core is significantly reduced in size after heat treatment, resulting in more uniform changes in the state of a "thin border and coarse core" [32].

#### 4.2 Dislocation evolution and its effects

CR and cold compression are two typical deformation behaviors; however, the metal flow during deformation differs. As described in Section 4.1, the metal flow is more concentrated during rolling and more dispersed during compression. According to the microscopic characteristics of polycrystal plasticity deformation, under low

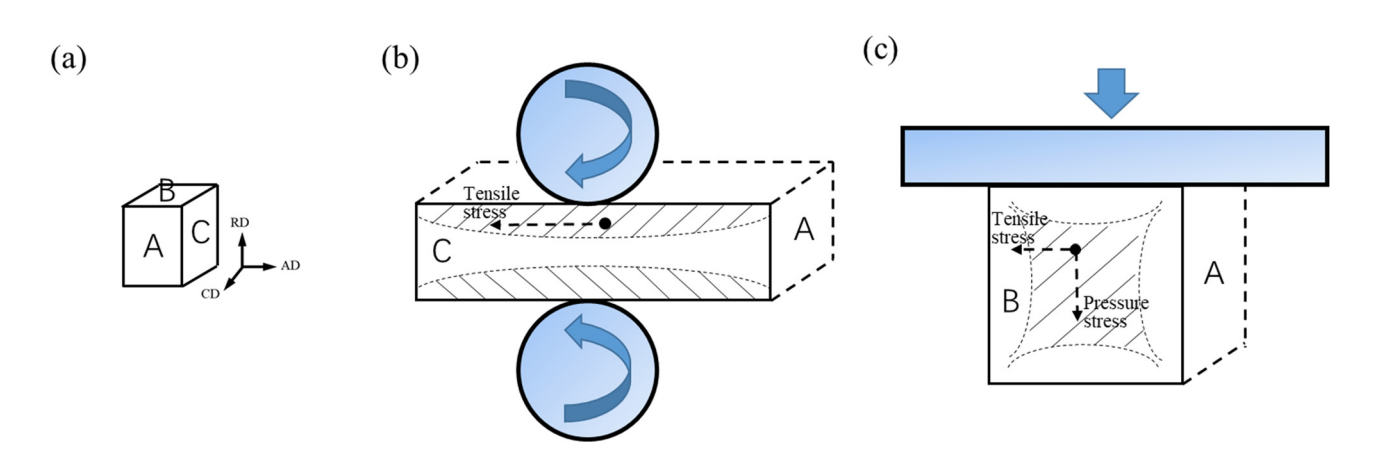


Figure 11: Deformation and stress characteristics. (a) Reference direction; (b) and (c) cold deformation under CR and cold compression, respectively.

temperatures, the internal dislocations glide mainly within the grain without crossing the grain boundary into the area adjacent to the grain. Thus, the material deformation modes determine the dislocation movement. Therefore, the dislocation distribution of the CR sample is relatively concentrated, with regions of high density and dislocation-free regions separated from each other. In contrast, the dislocation distribution is more dispersed in the cold-compressed sample. This phenomenon also increases the dislocation densities after CR deformation than after cold compression [33].

As shown in Figure 12, compared with the CR deformation, the metal flow direction under cold compression is more dispersed, with a shorter metal flow distance in the single direction [34]. The Al<sub>2</sub>Cu phase (blue circle in Figure 12) represents the stress concentration [35]. A large number of dislocations do not bypass the Al<sub>2</sub>Cu phase but tangle with the Al<sub>2</sub>Cu phases, continuing to accumulate in large quantities. During the subsequent solution treatment, a large number of dislocations can be used as atomic diffusion channels to fully expand the diffusion range of Cu atoms, thus improving the density of the precipitated phase of rings during aging [36,37]. Such dislocation accumulation process can also cause partial Al<sub>2</sub>Cu phase fragmentation, also contributing to the dissolution of Al<sub>2</sub>Cu phases. However, during the CR process, the metal flows quickly and in a certain direction. The Al<sub>2</sub>Cu phase is insufficient to cause the accumulation of a large number of dislocations.

## 4.3 Comparison of microstructure and mechanical properties

By increasing dislocation densities *via* cold deformation, the degree of grain refinement can be effectively improved by the elongation of the ring because of stronger interaction

between grain boundaries [21]. The more uniform grain structure induced by cold compression facilitates the extension of the alloy during the radial tensile process, resulting in better elongations [38].

In terms of tensile strength and yield strength, the range of increase under the two deformation modes is relatively similar. The yield strength mainly depends on the fine-grain strengthening and precipitation strength of the 2219 Al–Cu alloy [39]. The contribution of fine-grain strengthening to the yield strength can be expressed by the Hall-Petch relationship:

$$\Delta \sigma = \sigma_0 + \frac{k}{\sqrt{d}},\tag{4}$$

where  $\Delta\sigma$  is the yield strength, d is the average grain diameter, k and  $\sigma_0$  are constants. The value of k = 0.04 MPa·m<sup>1/2</sup> [39]. After calculation, the increase in yield strengths is calculated to be ~1 MPa as the grain diameter decreases from 113 to 198  $\mu$ m.

Precipitated phase characteristics are correlated with the material strength.  $\theta'$  phases are disk-like and non-shearable precipitate phases, and they improvise significantly towards the attainment of larger peak hardness by blocking dislocations efficiently. The size and quantity of the precipitates are deciding factors for influencing the strength of the material [40,41]. Orowan model indicated the following relationship between phases and shear-resistant:

$$\tau = \frac{Gb}{\lambda},\tag{5}$$

where  $\tau$  is the shear stress, G is the shear modulus, and b is the Burgess vector. The most critical factor in determining the yield strength is  $\lambda$ , which is the effective distance between precipitated phases.

Zhu and Starke [42] derived the following relationship between  $\theta$  phases and yield strengths under other constant conditions:

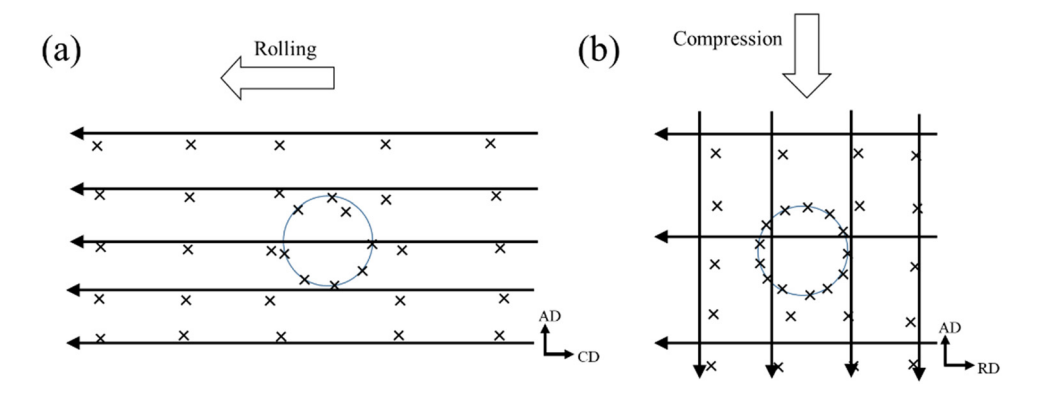


Figure 12: Comparison of Al<sub>2</sub>Cu phases and dislocation accumulation. (a) and (b) Cold deformation modes under CR and cold compression.

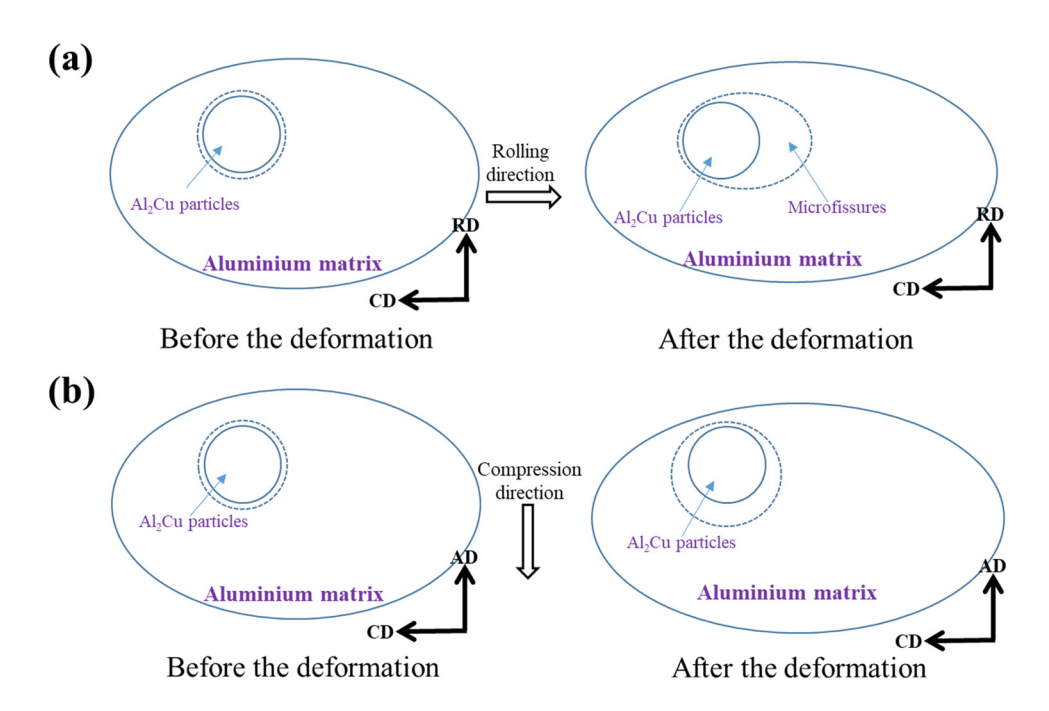


Figure 13: Comparison of Al<sub>2</sub>Cu phases and brittle fractures. (a) and (b) Cold deformation mode under CR and cold compression.

$$\Delta\sigma = 0.13MG \frac{b}{2\sqrt{rh}} \left[ f_{v}^{\frac{1}{2}} + 0.75 \left( \frac{r}{h} \right)^{\frac{1}{2}} f_{v} + 0.14 \left( \frac{r}{h} \right) f_{v}^{\frac{3}{2}} \right] \ln \left( \frac{0.158r}{r_{0}} \right),$$
(6)

where  $\Delta \sigma$  is the yield strength and r, h, and  $f_v$  are the diameter, thickness, and volume fraction of the  $\theta'$  phase, respectively, M is the Taylor factor, G is shear modulus, b. is Burgess vector, and  $r_0$  is the radius of the dislocation core near the  $\theta'$  phase [43]. The value of  $M = \sim 3.1$ , G = 27GPa,  $r_0 = \sim 4.5$  nm [44], and b = 0.286 nm. After calculation, when cold deformations are carried out, the increase in yield strengths is calculated to be ~14 MPa as the volume fraction and size of the  $\theta'$  phase change. The calculated yield strength of CR and cold compression sample is close. The effective distance of the  $\theta'$  phase is determined by the diameter, thickness, and volume fraction. The  $\theta'$  phase of the cold compression sample is denser (the distance between particles is smaller, reducing the effective distance), but with a larger width (when the dislocation bypasses the particle, the bigger the particle, the smaller the curvature radius of the dislocation movement, resulting in an increase in the effective distance), leading a relatively close effective distance [45,46].

In addition, the deformation resistance during cold deformation is large, resulting in local damage [47]. As shown in Figure 13, after the rolling process, the Al matrix moves around the coarse phase, and the moving distance

of the Al matrix differs in the circumferential and radial directions, resulting in larger microfissures around the coarse phase [48,49]. The microfissures in the tensile process under stress concentration may result in a local failure drastic fluctuation in mechanical properties [50,51] and reduction in the average mechanical properties [52,53]. Conversely, during cold compression, the similar circumferential and radial movements of the Al matrix around the coarse phase prevent local failures [54].

#### 5 Conclusions

The effects of cold deformation modes on the microstructure (dislocation accumulation, grain structures, and second-phase distribution), and their role in variations in mechanical properties of large 2219 Al–Cu alloy rings were studied. The main conclusions of this study are as follows:

- Compared with CR, cold compression causes a smaller increase in the dislocation density. However, the dislocation densities at the core are higher than in other areas, leading to a more uniform grain structure as well as uniform elongation in the axial and radial directions.
- 2) The CR deformation contributes to the dissolution of the coarse phase. The cold compression strongly contributes to the dissolution of the secondary phase, leading to denser and finer precipitates of cold-compressed

- samples, resulting in improved strength. Brittle fractures on the 5% CR samples reduce the mechanical properties due to the deformation mechanism of CR.
- 3) Deformation induced by both CR and cold compression can improve the mechanical properties of large rings, but the cold-compressed sample exhibits more uniform microstructures and higher comprehensive mechanical properties (the elongation increased from 7.1 to 11.2%; the IPA decreased from 36.6 to 8.9%) without brittle fractures.
- 4) The cold deformation with a small deformation amount adopted in this study is easier to realize in industrial large-ring manufacturing. This process has application prospects for mechanical properties improvement of other large components.

**Acknowledgments:** The authors acknowledge funding by the National Natural Science Foundation of China [grant number 52275267] and the National Natural Science Foundation of Hubei province [grant number 2022CFB617]. The authors thank Editage [www.editage.cn] for English language editing.

**Funding information:** This study was funded by the National Natural Science Foundation of China [grant number 52275267] and the National Natural Science Foundation of Hubei pro-vince [grant number 2022CFB617].

**Author contributions:** All authors have accepted responsibility for the entire content of this manuscript and approved its submission.

**Conflict of interest:** The authors state no conflict of interest.

**Data availability statement:** The datasets generated and/ or analyzed during the current study are available from the corresponding author on reasonable request.

## References

- [1] He, H. L., Y. P. Yi, S. Q. Huang, and Y. X. Zhang. An improved process for grain refinement of large 2219 Al alloy rings and its influence on mechanical properties. *Journal of Materials Science & Technology* (Shenyang, China), Vol. 35, 2019, pp. 55–63.
- [2] Mao, X. C., H. L. He, and Y. P. Yi. Second phase particles and mechanical properties of 2219 aluminum alloys processed by an improved ring manufacturing process. *Materials Science &*

- Engineering, A: Structural Materials: Properties, Microstructure and Processing, Vol. 781, 2020, id. 139226.
- [3] Guo, W. F., Y. P. Yi, and S. Q. Huang. Effects of deformation temperature on the evolution of second-phase and mechanical properties of large 2219 Al-Cu alloy rings. *Materials Characterization*, Vol. 160, 2020, id. 110094.
- [4] Shaterani, P., A. Zarei-Hanzaki, S. M. Fatemi-Varzaneh, and S. B. Hassas-Irani. The second phase particles and mechanical properties of 2124 aluminum alloy processed by accumulative back extrusion. *Materials & Design*, Vol. 58, 2014, pp. 535–542.
- [5] Kaibyshev, R., O. Sitdikova, I. Mazurina, and D. R. Lesuer. Deformation behaviour of a 2219 Al alloy. *Materials Science & Engineering, A: Structural Materials: Properties, Microstructure and Processing*, Vol. 334, No. 1, 2002, pp. 104–113.
- [6] Seo, H. Y., R. L. Jiang, G. K. Chung, and J. K. Chul. Effect of compression process of mwcnt-reinforced al6061 powder on densification characteristics and its mechanical properties. *Metals*, Vol. 7, No. 10, 2017, id. 437.
- [7] Li, H. J., Z. Y. Jiang, D. B. Wei, and X. J. Gao. Surface asperity evolution and microstructure analysis of Al 6061T5 alloy in a quasistatic cold uniaxial planar compression (CUPC). *Applied Surface Science A*, Vol. 347, 2015, pp. 193–201.
- [8] Lu, Y., Z. Xu, and X. Xu. The dynamic evolution of microstructure and mechanical properties of an Al-Cu-Li alloy during multi-axial compression. *Journal of Materials Research and Technology*, Vol. 14, 2021, pp. 2513–2521.
- [9] Dong, F., Y. P. Yi, and S. Q. Huang. Influence of cryogenic deformation on second-phase particles, grain structure, and mechanical properties of Al–Cu–Mn alloy. *Journal of Alloys and Compounds*, Vol. 827, 2020, id. 154300.
- [10] Li, Z. Z., H. G. Yan, J. H. Chen, W. J. Xia, and H. Z. Zhu. Enhancing damping capacity and mechanical properties of Al-Mg alloy by high strain rate hot rolling and subsequent cold rolling – sciencedirect. *Journal of Alloys and Compounds*, Vol. 908, No. 5, 2022, id. 164677.
- [11] Kazemi-Navaee, A., R. Jamaati, and H. J. Aval. Asymmetric cold rolling of AA7075 alloy: The evolution of microstructure, crystallographic texture, and mechanical properties. *Materials Science & Engineering, A: Structural Materials: Properties, Microstructure and Processina*. Vol. 824, 2021. jd. 141801.
- [12] Changela, K., H. Krishnaswamy, and R. K. Digavalli. Development of combined groove pressing and rolling to produce ultra-fine grained al alloys and comparison with cryorolling. *Materials Science & Engineering, A: Structural Materials: Properties, Microstructure and Processing*, Vol. 760, No. 8, 2019, pp. 7–18.
- [13] Immanuel, R. J., S. K. Panigrahi, and C. James. Malas Chapter 5-Materials development for sustainable manufacturing. Sustainable Manufacturing Processes, Vol. 5, 2023, pp. 155–194.
- [14] Fujita, S., H. Sato, and S. Motozuka. Deformation type during the ball milling process: A comparative study of the microstructures formed by ball milling, uniaxial compression, and rolling. *Powder Technology*, Vol. 426, No. 1, 2023, id. 118598.
- [15] Zecevic, M., M. Knezevic, I. J. Beyerlein, and R. J. McCabe. Texture formation in orthorhombic alpha-uranium under simple compression and rolling to high strains. *Journal of Nuclear Materials*, Vol. 473, 2016, pp. 143–156.
- [16] Lan, J., Z. Han, and L. Hua. Effects of cold deformations on strength and ductility of extruded Al-Cu-Mg-Si alloy. *Materials Letters*, Vol. 300, No. 3, 2021, id. 130188.

- [17] Guo, W. F., H. L. He, Y. P. Yi, S. Q. Huang, X. C. Mao, and J. Fang. Effects of axial cold-compression on microstructure uniformity and mechanical property enhancement of large 2219 Al-Cu alloy rings. *Materials Science & Engineering, A: Structural Materials: Properties, Microstructure and Processing*, Vol. 798, No. 4, 2020, id. 140233.
- [18] Guo, W. F., Y. P. Yi, S. Q. Huang, X. C. Mao, and J. Fang. Manufacturing large 2219 Al–Cu alloy rings by a cold rolling process. *Materials and Manufacturing Processes*, Vol. 35, 2020, pp. 291–302.
- [19] Youssef, K. M., R. O. Scattergood, K. L. Murty, and C. C. Koch. Nanocrystalline Al–Mg Alloy with ultrahigh strength and good ductility. *Scripta Materialia*, Vol. 54, No. 2, 2006, pp. 251–256.
- [20] Xu, X. J., J. Q. Cao, X. N. Cheng, and J. P. Mo. Tensile properties of 2024 Al alloy processed by enhanced solid-solution and equalchannel angular pressing. *Chinese Journal of Nonferrous Metals*, Vol. 35, No. s2, 2006, pp. 395–397.
- [21] Feng, Y. F., X. Chen, Y. Q. Hao, and B. Chen. Ageing evolution process of the -phase in Al-Si-Cu-Mg alloys: Atomic-scale observations and first-principles calculations. *Journal of Alloys and Compounds*, Vol. 968, 2023, id. 171787.
- [22] Niu, G. D., L. J. Zhu, W. R. Ren, and Y. Wang. Elevated temperature microstructural stability in Al-7Cu-0.5Mn-0.2Zr alloys through Ce addition: Enhanced coherent interfacial stability of cu-rich  $\theta'/\alpha$ -Al interface. *Materials Characterization*, Vol. 200, 2023, id. 112908.
- [23] Guo, W. F., Y. P. Yi, S. Q. Huang, and H. L. He. Effects of warm rolling deformation on the microstructure and ductility of large 2219 Al-Cu alloy rings. *Metals And Materials International*, Vol. 26, 2020, pp. 56–68.
- [24] Huang, J. W., Y. P. Yi, and S. Q. Huang. Effects of cryogenic deformation on second-Phase Al<sub>2</sub>Cu particles and mechanical properties of 2219 Al–Cu alloy rings. *Metals And Materials International*, Vol. 27, 2021, pp. 815–824.
- [25] Sharma, V. M. J., K. S. Kumar, B. N. Rao, and S. D. Pathak. Effect of microstructure and strength on the fracture behavior of AA2219 alloy. *Materials Science and Engineering A*. Vol. 502, No. 1–2, 2009, pp. 45–53.
- [26] Günen, A., S. Bayar, and M. S. Karakaş. Effect of different arc welding processes on the metallurgical and mechanical properties of RAMOR 500 armor steel. *Journal of Engineering Materials and Technology*, Vol. 142, No. 2, 2019, pp. 1–23.
- [27] Günen, A., B. Kurt, İ. Somunkıran, E. Kanca, and N. Orhan. The effect of process conditions in heatassisted boronizing treatment on the tensile and bending strength characteristics of the AISI304 austenitic stainless steell. *The Physics of Metals and Metallography*, Vol. 116, 2015, pp. 896–907.
- [28] Chen, L. H., C. H. Liu, P. P. Ma, J. S. Yang, L. H. Zhan, and M. H. Huang. Strong in-plane anisotropy of creep ageing behavior in largely pre-deformed Al-Cu alloy: experiments and constitutive modeling. *International Journal of Plasticity*, Vol. 152, 2022, id. 103245.
- [29] Meyers, M. and K. Chawla. Mechanical behavior of materials, 2nd edn, Cambridge University Press, USA, 2009.
- [30] Qasaimeh, M., D. Ravoori, and A. Jain. Modeling the effect of in situ nozzle-integrated compression rolling on the void reduction and filaments-filament adhesion in Fused Filament Fabrication (FFF). *Multiscale Science and Engineering*, Vol. 4, 2022, pp. 37–54.
- [31] Shen, J., X. Chen, V. Hammond, L. J. Kecskes, S. N. Mathaudhu, K. Kondoh, et al. The effect of rolling on the microstructure and compression behavior of AA5083 subjected to large-scale ECAE

- 2017. *Journal of Alloys and Compounds*, Vol. 695, No. 25, 2017, pp. 3589–3597.
- [32] Li, X. C. Microstructure and metallographic map of aluminum alloy, Metallurgical Industry Press, China, 2010.
- [33] Yu, S. W., X. L. An, and S. N. M. Song. Effects of temperature and loading direction on deformation mechanism of Ti-10at%Al alloy subjected to rolling and high speed compression. *Journal of Alloys* and Compounds, Vol. 925, 2022, id. 166801.
- [34] Li, F., G. N. Chu, and X. J. Liu. Deformation division of metal flow behavior during extrusion process of 7075 aluminum alloy. *Chinese Journal of Nonferrous Metals*, Vol. 16, No. 5, 2009, pp. 738–742.
- [35] Liu, Q., F. G. Qi, Q. H. M. Wang, and K. Y. Ding. The Influence of particles size and its distribution on the degree of stress concentration in particulate reinforced metal matrix composites. *Materials Science & Engineering, A: Structural Materials: Properties, Microstructure and Processing*, Vol. 731, No. 25, 2018, pp. 351–359.
- [36] Zuo, J. R., L. G. Hou, J. T. Shi, H. Cui, L. Z. Zhuang, and J. S. Zhang. The mechanism of grain refinement and plasticity enhancement by an improved thermomechanical treatment of 7055 Al Alloy. Materials Science & Engineering, A: Structural Materials: Properties, Microstructure and Processing, Vol. 702, 2017, pp. 42–52.
- [37] Vinod Kumar, G. S., B. S. Murty, and M. Chakraborty. Effect of TiAl3 particles size and distribution on their settling and dissolution behavior in aluminium. *Journal of Materials Science*, Vol. 45, 2010, pp. 2921–2929.
- [38] Thomason, P. F. A Three-dimensional model for ductile fracture by the growth and coalescence of microvoids. *Acta Metallurgica*, Vol. 33, No. 6, 1985, pp. 1087–1095.
- [39] Hansen, N. Hall-Petch relation and boundary strengthening. Scripta Materialia, Vol. 51, 2004, pp. 801–806.
- [40] Li, H., L. H. Zhan, M. H. Huang, and X. Zhao. unified constitutive model for multiphase precipitation and multi-stage creep ageing behavior of Al-Li-S4 alloy. *Transactions of Nonferrous Metals Society* of China, Vol. 31, 2021, pp. 1217–1234.
- [41] Ghosh, M., A. Miroux, and L. A. Kestens. Experimental study and modelling of the role of solutes, precipitates and temperature on the work-hardening of AA6xxx aluminium alloys. *Materials Science* and Engineering A, Vol. 805, 2021, id. 140615.
- [42] Zhu, A. W. and E. A. Starke. Strengthening effect of unshearable particles of finite size: a computer experimental study. *Acta Materialia*, Vol. 47, No. 11, 1999, pp. 3269–3269.
- [43] Wang, S. C. and M. J. Starink. Precipitates and intermetallic phases in precipitation hardening Al–Cu–Mg–(Li) based alloys. *International Materials Reviews*, Vol. 50, No. 4, 2005, pp. 193–215.
- [44] Medlin, D. L., N. Yang, and C. D. Spataru. Unraveling the dislocation core structure at a van der Waals gap in bismuth telluride. *Nature Communications*, Vol. 10, 2019, id. 1820.
- [45] Ambriz, R. R. and D. Jaramillo. Mechanical behavior of precipitation hardened aluminum alloys welds. *Light Metal Alloys Applications*, Vol. 1, 2014, pp. 2–5.
- [46] Fribourg, G., Y. Bréchet, A. Deschamps, and A. Simar. Micorstructure-based modelling of isotropic and kinematic strain hardening in a precipitation-hardened aluminum alloy. *Acta Materialia*, Vol. 59, No. 9, 2011, pp. 3621–3635.
- [47] Ng, K. C. and H. L. Chen. Numerical modelling of brittle fracture using lattice particle method with applications to fluid structure interaction problems via SPH coupling. *Engineering Fracture Mechanics*, Vol. 289, No. 1, 2023, p. 109453.

- [48] Mbati, M., T. Gerasimov, and L. De Lorenzis. A review on phase-field models of brittle fracture and a new fast hybrid formulation. *Computational Mechanics*, Vol. 55, 2015, pp. 383–405.
- [49] Zhou, M. Z. Research of relationship between heat-treatment and fatigue property of Aerial 2E12 Aluminum Alloy, PhD, Central South University, 2010.
- [50] Wang, B. Effect of grain size and residual stress on fatigue properties of 2E12 aluminum alloy, M. A. Sc, Central South University, 2014.
- [51] Ma, G. H., R. X. Li, and R. D. Li. Effects of stress concentration on low-temperature fracture behaviour of A356 Alloy. *Materials Science* & Engineering, A: Structural Materials: Properties, Microstructure and Processing, Vol. 667, 2016, pp. 459–467.
- [52] Rahimi, M. N. and G. Moutsanidis. A smoothed particle hydrodynamics approach for phase field modeling of brittle fracture. *Computer Methods in Applied Mechanics and Engineering*, Vol. 398, No. 1, 2022, id. 115191.
- [53] Zhao, X. X., W. Zhang, C. Q. Wang, W. Liu, and C. J. Hang. Effect of the second-phase particle distribution on the brittle fracture behavior of Sn-3Ag-0.5Cu solder. *Journal of Electronic Materials*, Vol. 52, 2023, pp. 3394–3400.
- [54] Y., Zhao, Z. Q. Zhou, J. Bi, and C. L. Wang. Simulation of brittle fractures using energy-bond-based smoothed particle hydrodynamics, *International Journal of Mechanical Sciences*, Vol. 248, No. 15, 2023, id. 108236.